LA-UR- 00-2296

Nanosecond interferometric studies of surface deformations of dielectrics induced by laser irradiation

Scott R. Greenfield*, Joanna L. Casson, and Aaron C. Koskelo

Los Alamos National Laboratory, Los Alamos, NM 87545

ABSTRACT

Transient surface deformations in dielectric materials induced by laser irradiation were investigated with time-resolved interferometry. Deformation images were acquired at various delay times after exposure to single pulses (100 ps at 1.064 μm) on fresh sample regions. Above the ablation threshold, we observe prompt ejection of material and the formation of a single unipolar compressional surface acoustic wave propagating away from the ablation crater. For calcite, no deformation – either transient or permanent – is discernable at laser fluences below the threshold for material ejection. Above and below-threshold behavior was investigated using a phosphate glass sample with substantial near infrared absorption (Schott filter KG3). Below threshold, KG3 exhibits the formation of a small bulge roughly the size of the laser spot that reaches its maximum amplitude by ~5 ns. By tens of nanoseconds, the deformations become quite complex and very sensitive to laser fluence. The above-threshold behavior of KG3 combines the ablation-induced surface acoustic wave seen in calcite with the bulge seen below threshold in KG3. A velocity of 2.97±0.03 km/s is measured for the KG3 surface acoustic wave, very close to the Rayleigh wave velocity calculated from material elastic parameters. Details of the transient interferometry system will also be given.

Keywords: Ablation, Surface acoustic wave (SAW), Rayleigh wave, Photoacoustics, Laser ultrasonics, Interferometry

1. INTRODUCTION

Laser ablation has become a phenomenon of wide importance, both as an unwanted occurrence in the operation of high-power lasers, and as a highly versatile tool used in such widely varying applications as machining, analytical chemistry, and the synthesis of novel materials. In spite of its significance, laser ablation remains a less than fully understood process. This is at least partially due to the breadth of the phenomena involved in ablation. In order to gain further insight into the ablation process, we have studied the deformations that appear on the sample surface at times very close to material ejection.

Lasers beams, even those with a "top hat" mode, do not have a perfectly flat spatial intensity distribution that falls off instantly to zero at the edges. Since laser ablation is strongly intensity-dependent, the details of the ablation process can vary significantly over the spatial extent of the laser pulse. For the purposes of investigating the ablation process, this can be overcome by probing the observables of interest only within the region illuminated by the innermost part of the ablation pulse; i.e., where the intensity is fairly constant. Alternatively, the spatial variation of the observables can be quantified by imaging. To achieve this, we have created an imaging interferometer that is capable of measuring nanometer-scale out-of-plane surface deformations with roughly 100-ps time resolution. Lateral resolution of better than 10 μm allows us to image the deformations with high spatial resolution. The dimensions of the image area are typically an order of magnitude greater than those of the ablation pulse, allowing observation of surface acoustic waves (SAWs) and other deformations that occur outside the illuminated region.

Transient imaging interferometry has been applied to study surface morphology changes due to laser ablation by Furutani and coworkers.[1-4] These experiments were performed on polymer films in an ambient air atmosphere with ~10 ns temporal resolution and were capable of measuring deformations of a few tens of nanometers. The analysis of the interferograms was based on a simple measurement of fringe shifts, and did not appear to allow the construction of a full image of the deformation at all points on the interferogram. The transient interferometry apparatus that we have developed improves on the temporal resolution of their work by over two orders of magnitude, and on the out-of-plane spatial resolution by over one order of magnitude. Furthermore, a two-dimensional Fourier transform analysis of the data allows the entire image to be constructed.

* Correspondence: Email: greenfield@lanl.gov; Telephone: 505 667 8263

DISCLAIMER

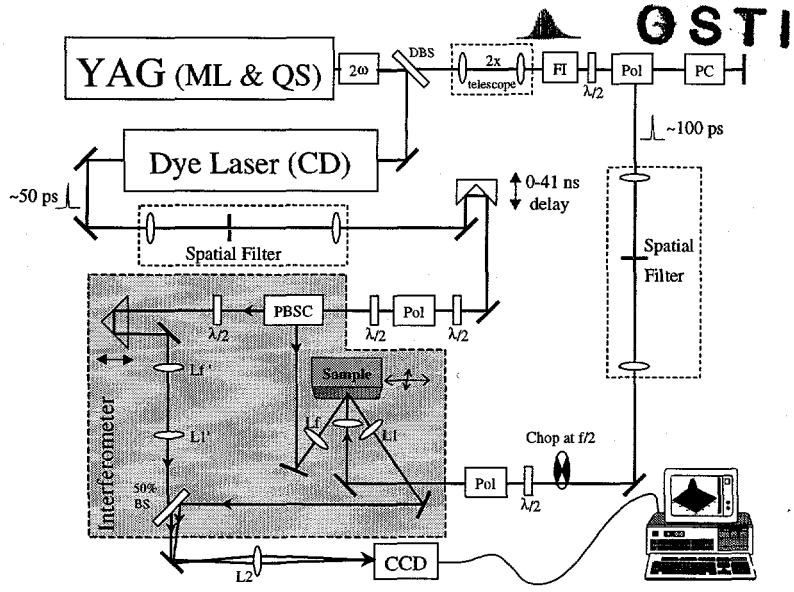

Figure 1. Transient interferometry apparatus. The shaded region shows the interferometer. YAG (ML & QS), mode-locked and Q-switched Nd:YAG laser; Dye Laser (CD), cavity-dumped dye laser; 2ω, CD*A frequency doubling crystal; DBS, dichroic beamsplitter; FI, Faraday Isolator; λ/2, half-wave plate; Pol, polarizer; PC, Pockels cell; PBSC, polarizing beamsplitter cube; BS, beamsplitter; CCD, CCD camera; Lx, lenses (see text for details).

The high temporal and spatial resolution of our apparatus allows for the observation of SAWs. The launching of acoustic waves from the interaction of a strong laser pulse with a surface was first observed by White.[5] Originally, the detection method for bulk and surface waves was a transducer; more recently, non-contact optical methods, including interferometry and probe beam deflection have become prevalent. The nature of these detection techniques, however, makes it difficult or impossible to measure the SAW as it is being launched. Such near field measurements may be advantageous for the study of the mechanisms of laser ablation. We believe this work represents the first time that a laser-generated SAW has been quantitatively imaged; i.e., the out-of-plane deformations of the SAW have been measured over a two-dimensional area.[6]

2. EXPERIMENT

2.1. Transient Interferometer

Transient interferometry is performed with the apparatus shown in Fig. 1. The output of a mode-locked and Q-switched YAG laser is frequency doubled with low efficiency to provide the pump light for the dye laser. The remaining fundamental is separated with a dichroic beamsplitter, and passes through a Faraday isolator. A calcite polarizer and a double-passed Pockels cell act as a pulse-picker, allowing a single pulse of roughly 100-ps length to be selected from the pulse train. The single pulse is spatially filtered, and focused onto the sample surface with an f_0=60 mm gradient index (GRIN) lens, providing a ~35-μm spot (diameter) at the sample surface. A half-wave plate-polarizer pair permits variable attenuation of the pulse energy, allowing both the above- and below-threshold intensity regimes to be accessed. For simplicity, this pulse will be referred to as the deformation pulse for both the above- and below-threshold cases. The laser repetition rate (500 Hz) is dropped in half for the deformation beam by a mechanical chopper that blocks every other pulse.

The dye laser is pumped by roughly 200 μJ of the 532-nm pulse train. Rhodamine 6G is used as the dye, and an intracavity prism sets the wavelength to 570 nm. A calcite polarizer and a Pockels cell are used to extract a single pulse of roughly 50-ps length and a few microjoules energy. This pulse is spatially filtered and sent down a double-passed, computer-controlled 2.4-m optical delay line. The delay line allows variation of the probe and deformation pulse timing by 28 ns; the time range is further extended by another 13 ns by selecting an earlier pulse from the IR pulse train. Cross correlation measurements using the optical Kerr effect measured in CS_2 give an instrument response function of 135 ps full width at half maximum (FWHM), and also are used to determine t=0.

The dye laser pulse is used to illuminate the interferometer, which is a modified Mach-Zehnder design. A polarizing beamsplitter cube separates the two arms of the interferometer. This element is preceded by a half-wave plate, which allows for adjustment of the relative intensities of the two arms to compensate for different sample reflectivities and is set to maximize fringe modulation. The interferometer arm that interrogates the sample surface will be referred to as the probe; the other arm will be referred to as the reference. The probe arm is weakly focused onto the sample surface at an angle of 21.5° from the surface normal by an f_0=200 mm lens (L_f). Although the off-normal angle of incidence introduces some complications, it is critically important for investigating the above-threshold regime. The probe light reflected off of the sample surface is collected by an f_0=75 mm achromat (L_1).

The reference beam is delayed to match the timing of the probe, and a half-wave plate rotates its polarization back to *s*. The reference beam passes through lenses L_f' and L_1'. These lenses are identical to those in the probe arm, and are placed in analogous positions to roughly match the wavefronts of the two interferometer arms. The recombination of the two arms, which is purposefully misaligned in the horizontal plane, is done with a 50% beamsplitter. The two beams pass through another achromat lens (L_2) that images the sample surface onto the CCD element. Two different focal lengths for L_2 were

used: f_0=150 mm (giving a 314x284-μm field-of-view of the sample surface), and f_0=50 mm (a 71x66-μm field-of-view). The anisotropy in the field-of-view is due to the off-normal angle of incidence of the probe beam on the sample surface.

A CCD camera (Photometrics PXL37) is used to record the interferograms. The camera has a frame transfer CCD chip with a 512x512-pixel active area, a 12-bit dynamic range, and a 1.8-ms frame transfer time. For each deformation event, a sequence of three images is recorded as follows. A background interferogram of the undeformed sample surface is recorded (the deformation pulse is blocked by the mechanical chopper for this cycle of the laser output). On the next laser cycle (i.e., 2 ms later), both the deformation and probe pulses hit the sample, with the probe pulse arriving at a set time that is variable from roughly 300 ps before the deformation pulse to 41 ns thereafter. This forms the dynamic image. A third interferogram is acquired several seconds later (with the deformation pulse again blocked by the chopper), providing a record of any permanent damage to the sample surface, e.g., an ablation crater. The triggers to the Pockels cells used to switch out the deformation and interferometry pulses are suppressed other than for the specific pulses discussed above, and mechanical shutters are used to block the weak leakage of the suppressed pulses through the Pockels cells. Of course, any leakage from the Q-switched pulse train out of which the actual deformation pulse is extracted could not be blocked by the shutter. Although it cannot be ruled out that this would result in a small local increase in sample temperature beyond the ambient value, it was determined that this leakage is too weak to produce any discernable deformations in either sample.

A single deformation event thus provides an image of any out-of-plane surface deformations at a single time delay after the deformation pulse. A time sequence is constructed by recording dynamic interferograms at different time delays, with all data acquired on fresh sample regions. Typically, 5-10 interferograms were recorded at each time delay; error bars on the figures are the standard deviations of those measurements.

The samples were mounted in a small vacuum chamber attached to a pair of translation stages. The sample was aligned such that its surface was parallel to the plane of motion of the two translation stages. This allowed the sample surface to be rastered without changing the focusing of the deformation beam or the alignment of the probe beam. Reported pulse energies were measured before the vacuum chamber; intensities take reflection losses into account. A mechanical pump was used to bring the sample chamber pressure down to roughly 15 mTorr.

2.2. Analysis

The misalignment at the interferometer exit creates a sinusoidal interference fringe pattern at the CCD. The fringe frequency is set to be quite high, with roughly five pixels between peaks. The Fourier transform spatial carrier frequency analysis of the interferograms follows the work of Takeda *et al.*[7] and subsequent improvements thereupon.[8] Briefly, an FFT is applied to the image. The resulting image has three distinct peaks: at DC, and at $\pm f_0$ (f_0 being the carrier frequency of the fringe pattern). One of the two $\pm f_0$ peaks is isolated with a filter, with the area outside the filter set to zero. The retained f_0 peak is then shifted to DC, and an inverse FFT is applied to the image. The complex logarithm of the image is then taken, the resulting imaginary part of which is the phase $\phi(x,y)$ at every pixel of the image. The phase thus determined is equivalent to the arctangent of the ratio of the imaginary and real parts of the argument of the logarithm; as such, the phase is wrapped into the range $-\pi$ to $+\pi$. The phase is unwrapped (i.e., the 2π-discontinuities removed) by adding the appropriate integer multiple of 2π at every pixel using the simple unwrapping algorithm of Takeda *et al.*[7] The phase is then converted to the surface displacement d by

$$d = \phi\lambda/4\pi\cos\theta\,, \tag{1}$$

where λ is the wavelength of the interferometry (i.e., dye) laser and θ is the angle of incidence. The fully analyzed background image is subtracted from both the dynamic and infinite-time images, which eliminates any pre-existing surface features on those images. A further result of the background subtraction is that it alleviates the need to carefully match the probe and reference wavefronts, as any mismatch is identical for all interferograms and is therefore removed by the subtraction.

2.3. Samples

Two materials were examined, calcite and the Schott filter glass KG3, which serve as examples of transparent and absorbing dielectrics, respectively. Calcite, the crystalline form of calcium carbonate ($CaCO_3$), has a bandgap of 5.9 eV, well above the energy of the 1.16-eV ablation photons. The actual calcite sample was the inner face of an air-gap polarizer. The absorption that initiates the dielectric breakdown leading to ablation is presumably due to defects, the existence of which are enhanced by polishing.[9] KG3 is a phosphate glass (P_2O_5) that absorbs strongly in the near IR ($\alpha_{1.06\,\mu m} = 16\ cm^{-1}$).

3. RESULTS AND DISCUSSION

3.1. Shock Wave Formation in Air

Experiments performed in an ambient air atmosphere indicate the formation of a shock wave. Figure 2 shows the radius of the outer edge of the shock wave as a function of delay time for calcite ablation; the inset shows the $t^{0.4}$ dependence expected for a spherical shock front.[10] Although the ablation crater becomes visible within a few nanoseconds of the deformation pulse, the phase shift from the shock front and the plume are sufficient to mask any surface deformations other than the crater itself. The initial velocity of the shock front is in excess of mach 30, dropping rapidly to roughly mach 5 by 40 ns.

3.2. Above-threshold Deformations: Calcite

Reduction of the pressure to roughly 15 mTorr completely impedes the formation of the shock front. As with the case of ambient atmosphere, an optical phase change in the region of the ablation spot begins to appear during the deformation pulse. This phase change is clearly different from that seen in the below threshold regime, and indicates that ablation begins during the ~100-ps deformation pulse. At reduced pressure, the plume of ablated material moves away from the crater at substantially greater velocity than at ambient pressure,[11, 12] and disappears from the field-of-view by roughly 2 ns, with the exact value depending on the choice of L_2. This indicates that the upper limit for the end of material ejection is 2 ns. It probably ends much earlier; this is the time when the last of the ejecta are roughly 90 μm away from the surface (for L_2 = 50 μm).

As soon as the plume has passed outside of the field-of-view, the crater resulting from the ablation becomes visible. Figure 3 shows the depth of the crater as a function of time after the arrival of the deformation pulse. As discussed above, interference from the plume makes the first such measurement impossible until a few nanoseconds after the deformation pulse. At 3-4 ns, the measured depth of the crater is over twice that seen at later times. This greater apparent depth is at least partially due to overlap with the compressional SAW that is forming at this time. By ~6 ns, the crater has reached a depth that is virtually indistinguishable from that seen at infinite time.

Figure 4 shows the surface deformations for calcite at 30 ns. The ablation crater is visible in the center. Also visible is a SAW. This SAW is a unipolar compressional pulse; i.e., it appears as a "dent" in the surface. The ellipticity of the SAW – 1.21, with the effect of the off-normal angle of incidence removed – is due to the anisotropy of the calcite crystal. Images at other times indicate that the SAW remains quite narrow (~10 μm wide), and undergoes little change in shape with time.

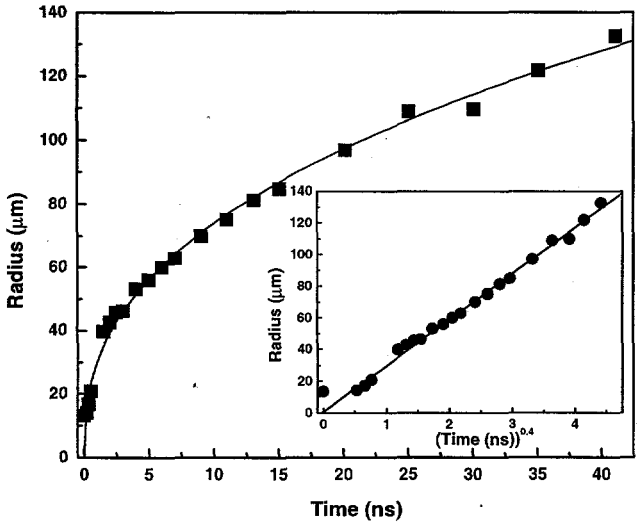

Figure 2. Radius of the outer edge of the shock wave formed in air due to ablation of calcite with 75-μJ pulses. The line is the fit to the $t^{0.4}$ radial dependence anticipated for a spherical shock. Inset shows the data plotted as a function of $t^{0.4}$, with linear fit.

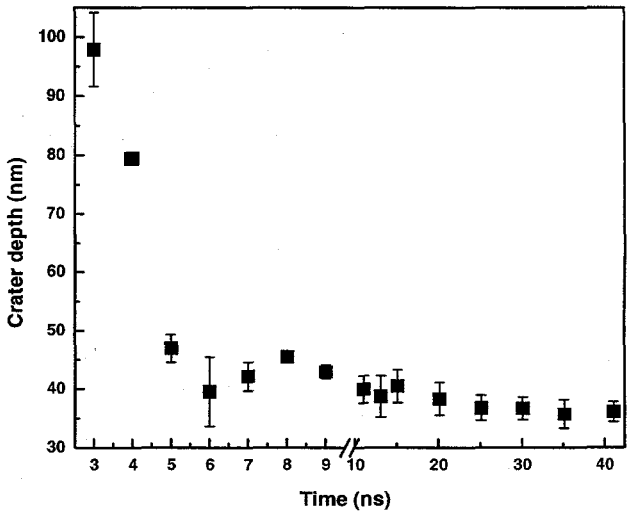

Figure 3. Depth of the ablation crater for calcite in vacuum as a function of time after the 75-μJ deformation pulse. Between 3-4 ns, the developing SAW overlaps with the crater. By roughly 6 ns, the crater has reached its infinite-time dimensions. Note the change in scale in the *x*-axis at 10 ns.

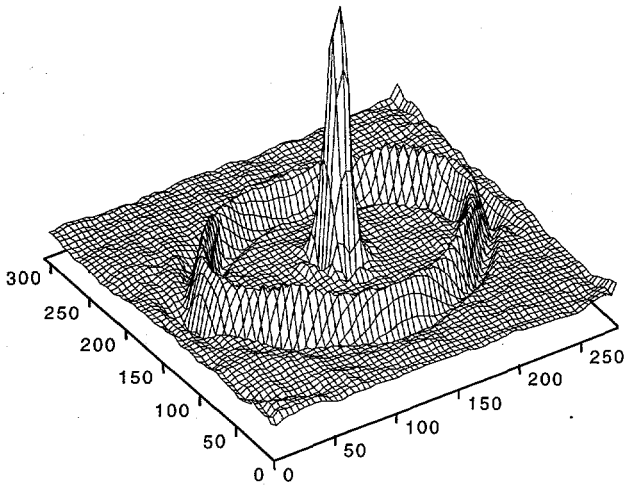

Figure 4. Crater and SAW in calcite at 30 ns after the 75-μJ deformation pulse, measured in vacuum. Both the crater and SAW are depressions; i.e., the view is as if from *inside* the sample. Lateral dimensions are in microns; crater depth is ~40 nm.

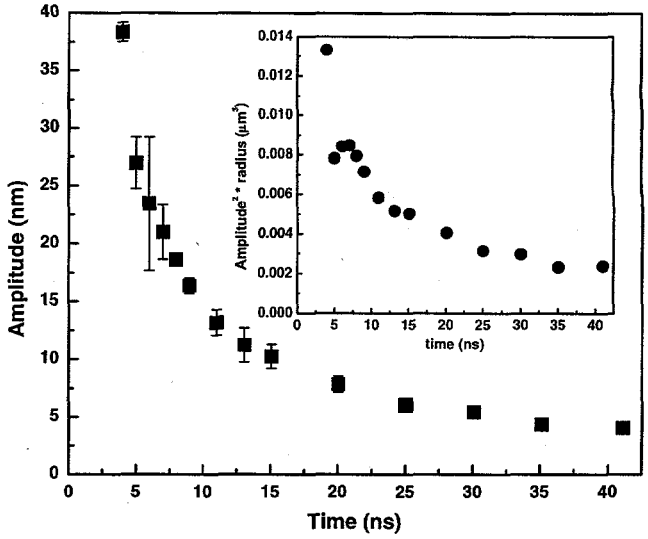

Figure 5. Peak amplitude of the SAW in calcite as a function of time after the 75-μJ deformation pulse, measured in vacuum. Inset shows the square of the amplitude multiplied by the radius; this quantity would be constant if a Rayleigh wave propagated without loss in the far field (see text).

Figure 5 shows the amplitude of the SAW as a function of time. The amplitude rapidly drops from almost 40 nm at 4 ns to less than 5 nm at 40 ns. As the radius of the SAW increases, the energy of the wave must spread over an area that increases linearly with the radius. To get an idea of the attenuation of the SAW as it propagates, we have also plotted the square of the SAW's amplitude multiplied by its radius as a function of time. This quantity should be proportional to the total energy of the SAW, and would remain constant with time if the SAW were to propagate without loss. As the inset clearly shows, the SAW undergoes significant (apparent) attenuation during its first 41 ns.

The origin of the faster-than-expected amplitude decrease may well not be true attenuation. Energy conservation predicts that the amplitude of a Rayleigh wave launched from a point source propagating without loss would have an $r^{-1/2}$ radial dependence. For a Rayleigh wave emanating from an extended-width source, Doyle has shown that this $r^{-1/2}$ dependence is valid only in the far field. When the radius of the SAW is less than roughly five times the radius of the laser spot, the drop-off is steeper than $r^{-1/2}$.[13] As all of the measurements presented here were made in the near field regime ($r_{SAW}/r_{laser}<5$), the quantity plotted in the inset to Fig. 5 would be expected to decrease with time.

Another source of apparent attenuation may be overlap with bulk acoustic waves at early times. The velocity of the bulk longitudinal wave is sufficiently greater than that of the Rayleigh wave that it would already be spatially separated from the Rayleigh wave by roughly 5 ns. The bulk shear wave, however, is only slightly faster than the Rayleigh wave (see section 3.4), and a noticeable spatial separation of 10 μm would not be achieved until a few tens of nanoseconds. By this time, however, the shear wave amplitude might be too low to be noticed, as the amplitude of bulk waves at the surface drops as r^{-2}. It is therefore possible that the SAW measured at early time has significant contribution from a rapidly decaying bulk shear wave. Of course, some degree of true attenuation of the SAW (i.e., loss) cannot be ruled out.

3.3. Below-threshold Deformations: KG3

No transient deformations were observed with calcite below the threshold for ablation. Once defect-driven absorption has led to dielectric breakdown, sufficient laser energy is absorbed to induce ablation. Below the threshold for dielectric breakdown, only a tiny amount of energy is absorbed – far to little to cause any detectable deformation. In order to investigate the behavior of transient deformations below the threshold for material ejection (i.e., ablation), we have used KG3 as a sample. The absorption coefficient of KG3 at the wavelength of the deformation pulse is 16 cm^{-1}. Therefore, the absorption per micron is only 0.4%. Although the absorption near the surface is quite small (almost trivial compared to a metallic sample), it is sufficient to induce prominent transient deformations below the threshold for material ejection.

Figure 6 shows the surface deformation for KG3 at 4 ns after the arrival of the deformation pulse. The deformation appears as a bulge with a peak height of ~30 nm and a FWHM of ~17 μm. This feature is presumably due to thermoelastic expansion

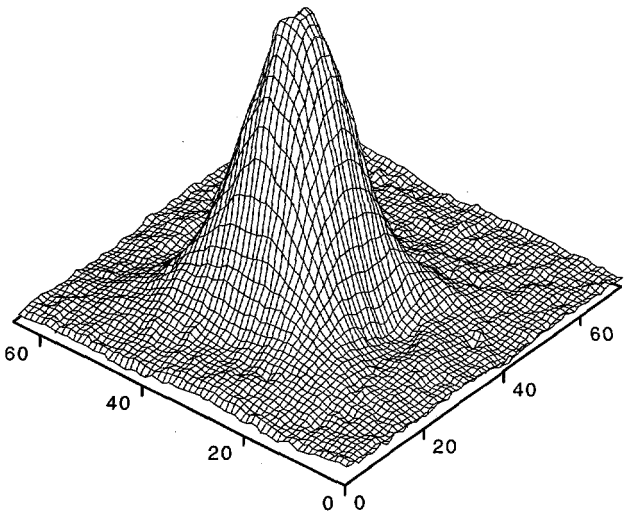

Figure 6. Transient surface deformation in KG3 at 4 ns due to a 50-μJ deformation pulse, measured in vacuum. The deformation appears as a bulge; i.e., the view is as if from *outside* the sample. Lateral dimensions are in microns; the peak amplitude of the bulge is ~30 nm.

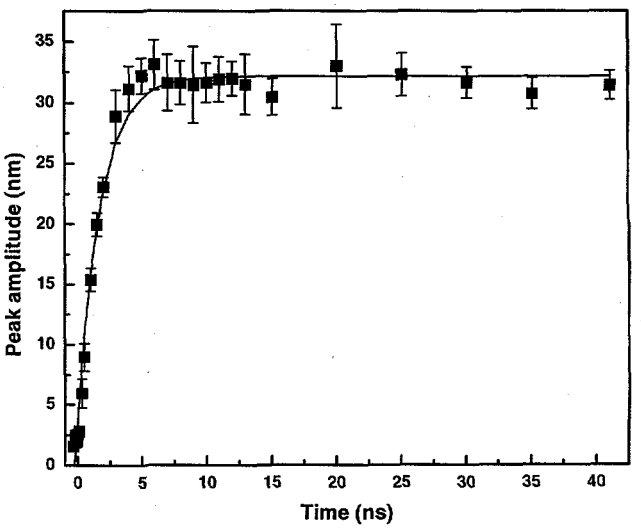

Figure 7. Peak amplitude of the transient bulge in KG3 as a function of time after the 50-μJ deformation pulse, measured in vacuum. The solid line is a single exponential fit to the rise with a time constant of 1.8 ns.

of the sample region directly heated by the deformation pulse. No permanent deformation is visible with the interferometry apparatus several seconds later; the lack of permanent surface deformation has been confirmed by atomic force microscopy (AFM). Figure 7 shows the peak of the deformation as a function of time after the deformation pulse. The peak amplitude is reached by roughly 5 ns; the solid line shows a single-exponential fit to the rise with a time constant of 1.8 ns.

The peak amplitude and the volume of the bulge as a function of laser energy at 5 ns are shown in Figs. 8a and 8b, respectively. Both parameters depend linearly on the laser energy, as the fits clearly show. These linear fits combined with an *x*-axis intercept at zero pulse energy indicate the linear nature of the absorption of the laser light. Nonlinear absorption would be manifest as either an *x*-axis intercept at nonzero pulse energy and/or a nonlinear dependence on pulse energy. The data at the highest measured pulse energy appears to be farther off of the linear fit than the other data points. It is possible that ablation that is too weak to be detected by the experimental apparatus may be occurring at this energy. AFM measurements indicate that very small craters are not detected by the transient interferometer (see section 3.4). The energy

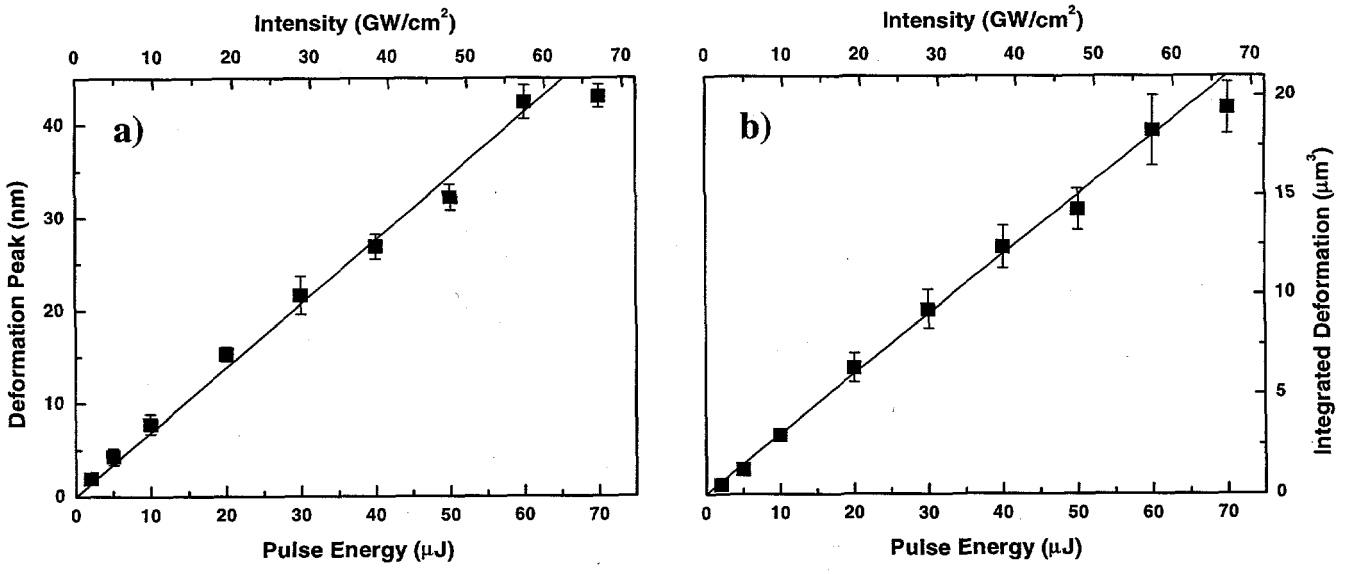

Figure 8. Parameters of transient bulge in KG3 as a function of laser energy measured at 5 ns in vacuum. The highest-energy data point was excluded from the linear fits. (a) Peak amplitude. (b) Volume.

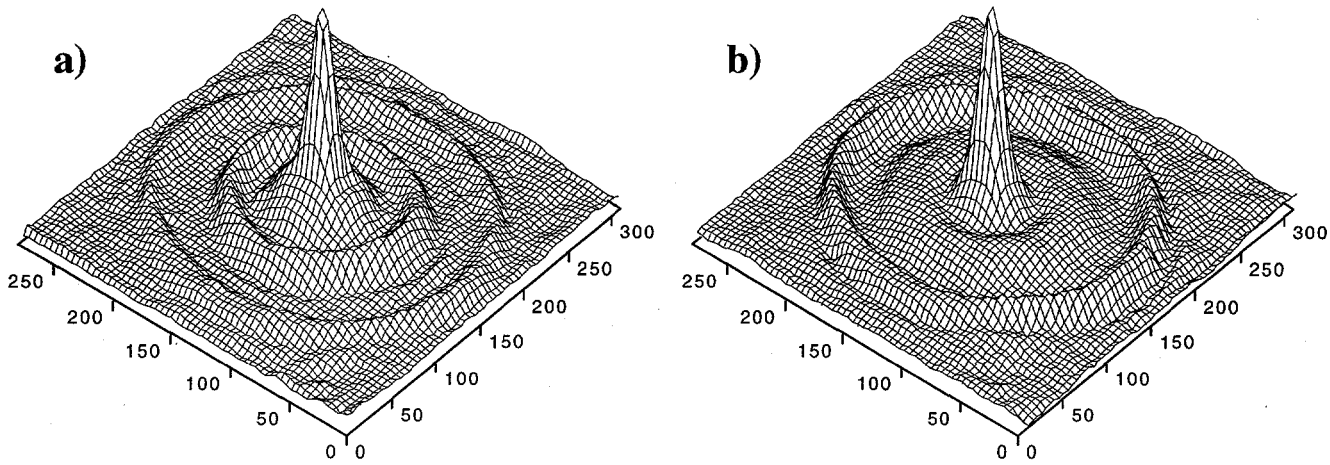

Figure 9. Transient deformations in KG3 at 25 ns, measured in vacuum. The deformations appear as a bulge; i.e., the view is as if from *outside* the sample. The two images are from nominally identical-energy laser pulses (75 μJ). Note the difference in the amplitude of the outer SAW, and the difference in the inner region (a strong, narrow SAW in (a) *vs.* a weak, broad SAW in (b)). Lateral dimensions are in microns; the peak amplitude of the central bulge for both is roughly 50 nm.

required for weak ablation would of course not be available for thermal expansion, resulting in a bulge that is smaller than expected.

Little or no change in the central region of the bulge is seen after the peak amplitude is reached. However, the outer region of the bulge and the surrounding area experience complex behavior on a tens of nanoseconds time scale that is highly dependent on laser fluence. By roughly 6 ns, the wings of the bulge begin to rise, presumably due to thermoelastic expansion caused by thermal diffusion away from the hot central region. At high fluence at 15 ns, this expansion in the wings of the bulge reaches an amplitude that is over one-third of the amplitude of the peak of the bulge and has a width (FWHM) of roughly 75 μm. Figure 9 shows the surface deformations at 25 ns for two different pulses at nominally identical fluences. As is clearly apparent, the nature of the deformations is quite complex and significantly different for the two events. There appears to be a strong correlation between the peak amplitude of the central bulge and the nature of the deformation. For the highest peak amplitudes (e.g., Fig. 9a), two sharp SAW pulses are observed. These SAWs separate from the central region at roughly 17 and 22 ns. At slightly lower peak amplitudes (e.g., Fig. 9b), only one narrow SAW is observed. Although this SAW has very close to the same radius as the outer one in Fig. 9a, it is of significantly greater amplitude. Instead of the strong inner SAW of Fig. 9a, there now appears to be a broad, weak SAW in the region surrounding the central bulge. At still lower deformation peak amplitudes, no SAWs are observed, only a pedestal surrounding the central bulge.

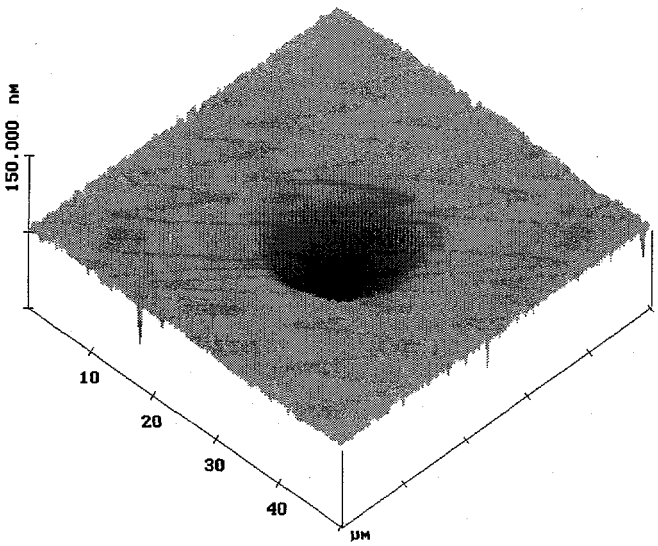

Figure 10. AFM image of crater in KG3 from a 75-μJ deformation pulse. Crater dimensions are depth: 66 nm; edge-to-edge width: 23 μm; FWHM: 13.3 μm.

3.4. Above-threshold Deformations: KG3

Figure 10 shows an AFM image of a typical crater created in KG3 in the above-threshold regime. The crater walls are quite smooth, and no debris is found near the edge. There is also no evidence of melting within the crater, indicative of the non-thermal nature of the ablation process. Dimensions of this crater are depth: 66 nm; edge-to-edge width: 23 μm; FWHM: 13.3 μm. Interferometric measurements of this same crater give a similar FWHM (12.5 μm), and a somewhat smaller depth (38 nm). This underreporting of the crater depth is due to the small amount of astigmatism that is present in the imaging optics. This limits the resolving power of the system to several times diffraction-limited, and conceals the smallest features – e.g., the tip of the crater. The astigmatism also puts a lower limit on the size of detectable craters; a

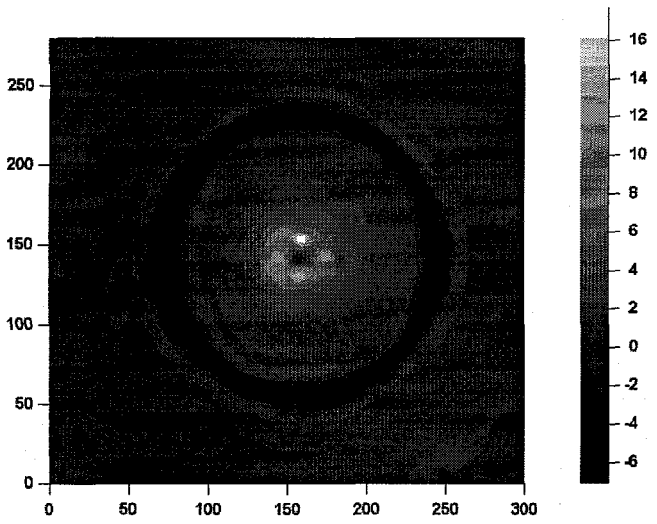

Figure 11. Surface deformations for KG3 at 30 ns after the 75-μJ deformation pulse, measured in vacuum. Lateral dimensions are in microns; out-of-plane displacements are indicated by gray-scale with units of nanometers.

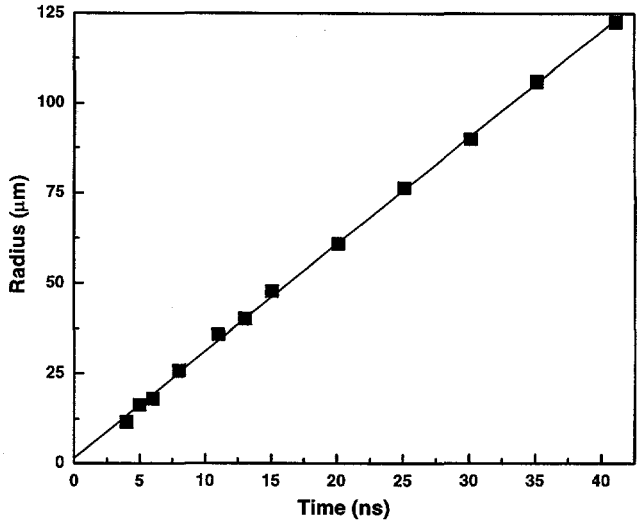

Figure 12. Radius of the SAW in KG3 as a function of time after the 75-μJ deformation pulse, measured in vacuum. The slope of the linear fit gives a SAW velocity of 2.97±0.03 km/s. Error bars (not shown) are of the same size or smaller than the symbols.

crater that was measured by AFM to be 22 nm deep and 2.6 μm FWHM was not detected by the transient interferometer.

Figure 11 shows the surface deformations for KG3 at 30 ns. As with the SAW generated in calcite (see Fig. 4), the SAW generated in KG3 is a unipolar compressional wave that undergoes little change in waveform with time. For the same crater depth, the SAW is also of similar amplitude to that generated in calcite. Of course, the ellipticity seen with calcite is absent with the isotropic phosphate glass sample.

The radial expansion of the KG3 SAW is shown in Fig. 12. The linear fit to the data gives a velocity for the SAW of 2.97±0.03 km/s. The velocity of a Rayleigh wave, V_R, can be estimated to within roughly 1% accuracy by[14]

$$V_R = \frac{0.862 + 1.14\nu}{1+\nu} V_S , \tag{2}$$

where V_S is the shear wave velocity and ν is Poisson ratio of the material. As the Poisson ratio varies over the physically real range of 0 to 0.5, the Rayleigh velocity increases from 86% to 96% of the shear velocity. The Poisson ratio relates the shear velocity and the longitudinal velocity, V_L, by

$$V_S / V_L = \sqrt{\frac{1-2\nu}{2-2\nu}} . \tag{3}$$

The longitudinal velocity can be calculated from material elastic parameters by

$$V_L = \sqrt{\frac{E(1-\nu)}{\rho(1+\nu)(1-2\nu)}} , \tag{4}$$

where E is the Young's modulus and ρ is the density. The pertinent elastic parameters for KG3 are E=6.8x10^4 N/mm^2, ρ=2.55 g/cm^3, and ν=0.22.[15] Using these parameters and equations 2-4 gives a Rayleigh velocity of 3.015 km/s – very close to the experimental value (a 1.5% error). It should be noted that this high degree of accuracy was achieved using only 1-3 interferograms per time point at all but three of the delay times.

Unlike the case with calcite, the craters formed with ablation of KG3 are not readily discernable in the dynamic interferograms. In fact, the net displacement in the central region for these dynamic data is *positive* – i.e., a bulge. This is readily explained by the directly-irradiated region being a superposition of the crater and the larger thermoelastic bulge. If it were not for the astigmatism resulting in a slight four-fold symmetry distortion of the crater shape, the expected pattern would be readily apparent. However, the effect of this distortion is to make the central region look somewhat like an Iron Cross. It is nevertheless possible to recreate the bulge without the crater and its resultant distortion by subtracting the

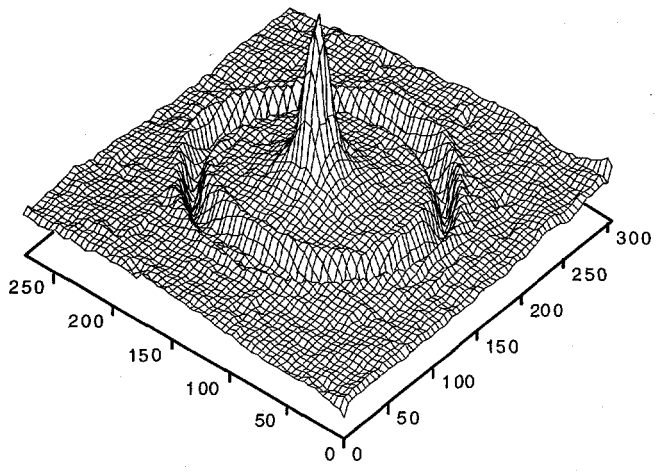

Figure 13. Surface deformations for KG3 at 30 ns after the 75-μJ deformation pulse, measured in vacuum. This is the data in Fig. 11 after subtraction of the infinite-time crater. The central deformation appears as a bulge; i.e., the view is as if from *outside* the sample. Lateral dimensions are in microns; the peak amplitude of the central bulge is ~35 nm.

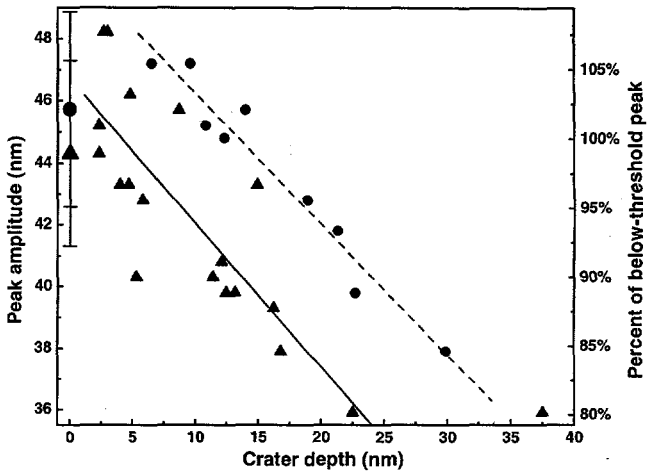

Figure 14. Peak amplitude of the thermoelastic bulge in KG3 measured at 25 ns in vacuum as a function of crater depth. The amplitude was measured after subtraction of the infinite-time crater (see text and Fig. 13). Triangles (▲) and circles (●) represent data acquired on two different days; solid and dashed lines are the linear fits to the data on those days. The data at zero crater depth is the average of below-threshold shots.

infinite-time data from the dynamic image. Inherent in this operation is the assumption that the crater dimensions have reached their infinite-time values in the dynamic data. For calcite, this was shown to be the case by roughly 6 ns (see Fig. 3). Although the thermoelastic bulge makes direct determination of this impossible in KG3, the distortion due to the astigmatism can actually be used to check this assumption. If the crater shape changes appreciably between the dynamic and infinite-time images, the distortion will also change and therefore will not be perfectly subtracted out. Hence, the presence of any four-fold symmetry distortion in the subtracted image can be used to determine if the crater changed shape between the dynamic image and the infinite-time image. No such distortion is seen after 6-8 ns, similar to the results for calcite.

Figure 13 shows the data from Fig. 11 with the infinite-time image subtracted out. Both the ablation recoil-generated SAW and the thermoelastic bulge can be clearly seen. None of the distortion discussed in the previous paragraph and seen in Fig. 11 is visible in the subtracted image.

The amplitude of the thermoelastic bulge as measured in the subtracted images for data at 25 ns is plotted as a function of infinite-time crater depth in Fig. 14. Data taken on two separate days are distinguished. The data points at zero crater depth correspond to the average of below-threshold shots (or ones producing craters too small to be seen by the transient interferometer, *vide supra*). Data points at finite crater depths are individual shots. Although there is a nontrivial amount of scatter in the data, the data for the two days clearly fit to parallel straight lines. The difference between the data for the two days may be due to a slight difference in the ablation beam focusing.

Even for the largest craters, the thermoelastic bulge remains quite substantial, never dropping below 80% of the below-threshold bulge amplitude. This clearly indicates that the ablation process for KG3 – with the laser pulses used in this experiment – never efficiently utilizes the laser energy. The vast majority of the energy is absorbed far from the surface and goes into bulk heating of the sample. This idea is confirmed by polarized optical microscope images, which reveal subsurface strain-induced birefringence for both above and below-threshold shots. If all of the laser pulse energy were channeled into the ablation process, neither the thermoelastic bulge nor the subsurface birefringence would be present.

4. CONCLUSION

We have examined the transient surface deformations of both a transparent dielectric and a strongly absorbing dielectric in response to irradiation by a tightly focused 100-ps laser pulse using transient interferometry. Above threshold, dielectric breakdown and possibly material ejection commence during the deformation pulse. In air and above threshold, a strong shock wave obscures the surface changes. In vacuum, the shock wave is not formed and the plume of ejected material passes out of the field of view by a few nanoseconds. The ablation crater is visible at this time, and reaches its infinite-time dimensions by roughly 6 ns in calcite. A strong unipolar SAW is observed propagating away from the ablation crater; the

SAW velocity in the phosphate glass KG3 closely matches that calculated for a Rayleigh wave based on the material's elastic parameters. The SAW appears as a depression, and propagates with little change in shape, although it does experience apparent attenuation. The below-threshold case was examined in KG3, where strong near infrared absorption can lead to substantial deformations without material ejection. A bulge somewhat narrower than the size of the deformation pulse reaches its peak amplitude by roughly 5 ns. By tens of nanoseconds, the deformations are quite complex and their features are strongly dependent on laser energy. The bulge persists in the above-threshold regime for KG3; amplitude measurements indicate that only a small fraction of the laser energy is utilized in the ablation process.

ACKNOWLEDGMENTS

The authors thank Drs. Marilyn Hawley (atomic force) and Robert Dickerson (optical) for the microscopy measurements on KG3. This work was partially supported by the Laboratory Directed Research and Development Program of Los Alamos National Laboratory, under the auspices of the U.S. Department of Energy. SRG acknowledges a J. Robert Oppenheimer postdoctoral fellowship.

REFERENCES

1. H. Furutani, H. Fukumura, and H. Masuhara, "Nanosecond time-resolved interferometric study on morphological dynamics of doped poly(methyl methacrylate) film upon laser ablation," *Appl. Phys. Lett.* **65**, pp. 3413-3415, 1994.
2. H. Furutani, H. Fukumura, and H. Masuhara, "Photothermal transient expansion and contraction dynamics of polymer films by nanosecond interferometry," *J. Phys. Chem.* **100**, pp. 6871-6875, 1996.
3. H. Furutani, H. Fukumura, H. Masuhara, T. Lippert, and A. Yabe, "Laser-induced decomposition and ablation dynamics studied by nanosecond interferometry. 1. A triazenopolymer film," *J. Phys. Chem. A* **101**, pp. 5742-5747, 1997.
4. H. Furutani, H. Fukumura, H. Masuhara, S. Kambara, T. Kitaguchi, H. Tsukada, and T. Ozawa, "Laser-induced decomposition and ablation dynamics studied by nanosecond interferometry. 2. A reactive nitrocellulose film," *J. Phys. Chem. B* **102**, pp. 3395-3401, 1998.
5. R. M. White, "Generation of elastic waves by transient surface heating," *J. Appl. Phys.* **34**, pp. 3559-3567, 1963.
6. S. R. Greenfield, J. L. Casson, and A. C. Koskelo, "Nanosecond interferometric studies of surface deformation induced by laser irradiation," *Proc. SPIE* **3902**, pp. 108-117, 2000.
7. M. Takeda, H. Ina, and S. Kobayashi, "Fourier-transform method of fringe-pattern analysis for computer-based topography and interferometry," *J. Opt. Soc. Am.* **72**, pp. 156-160, 1982.
8. M. Kujawinska, "Spatial phase measurement methods," in *Interferogram Analysis: Digital Fringe Pattern Measurement Techniques*, D. W. Robinson and G. T. Reid, Eds., Institute of Physics, Bristol, pp. 141-193, 1993.
9. R. L. Webb, S. C. Langford, and J. T. Dickinson, "The role of defects in the rear side laser ablation of MgO at 308 nm," *J. Appl. Phys.* **80**, pp. 7057-7064, 1996.
10. Y. B. Zel'dovich and Y. P. Raizer, *Physics of Shock Waves and High-Temperature Hydrodynamic Phenomena*, Academic Press, New York, 1966.
11. R. A. Lindley, R. M. Gilgenbach, C. H. Ching, J. S. Lash, and G. L. Doll, "Resonant holographic interferometry measurements of laser ablation plumes in vacuum, gas, and plasma environments," *J. Appl. Phys.* **76**, pp. 5457-5472, 1994.
12. H. Schittenhelm, G. Callies, P. Berger, and H. Hügel, "Time-resolved interferometric investigations of the KrF-laser-induced interaction zone," *Appl. Surf. Sci.* **110**, pp. 493-497, 1997.
13. P. A. Doyle, "Calculation of ultrasonic surface waves from an extended thermoelastic laser source," *J. Nondestr. Evaluation* **8**, pp. 147-164, 1989.
14. J. D. Achenbach, *Wave Propagation in Elastic Solids*, North Holland, Amsterdam, 1973.
15. R. J. Scheller, Schott Glass Technologies data.